



Terrestrial Bow Shock Parameters From MMS Measurements: Dependence on Upstream and Downstream Time Ranges

E. L M Hanson, O. Agapitov, F. Mozer, V. Krasnoselskikh, S. Bale, L. Avanov, B. Giles, R. Torbert

► To cite this version:

E. L M Hanson, O. Agapitov, F. Mozer, V. Krasnoselskikh, S. Bale, et al.. Terrestrial Bow Shock Parameters From MMS Measurements: Dependence on Upstream and Downstream Time Ranges. *Journal of Geophysical Research Space Physics*, 2020, 125 (1), 10.1029/2019JA027231 . insu-02524264

HAL Id: insu-02524264

<https://insu.hal.science/insu-02524264>

Submitted on 30 Mar 2020

HAL is a multi-disciplinary open access archive for the deposit and dissemination of scientific research documents, whether they are published or not. The documents may come from teaching and research institutions in France or abroad, or from public or private research centers.

L'archive ouverte pluridisciplinaire **HAL**, est destinée au dépôt et à la diffusion de documents scientifiques de niveau recherche, publiés ou non, émanant des établissements d'enseignement et de recherche français ou étrangers, des laboratoires publics ou privés.



JGR Space Physics

TECHNICAL REPORTS: DATA

10.1029/2019JA027231

Key Points:

- We selected and processed 51 quasi-perpendicular crossings of the terrestrial bow shock seen by the Magnetospheric Multiscale mission
- We analyzed the stability of the shock parameters based on different upstream and downstream regions
- We offer guidelines for defining stream regions; summary plots and detailed tables of parameters are available in the supporting information

Supporting Information:

- Supporting Information S1

Correspondence to:

E. L. M. Hanson,
lily.hanson@berkeley.edu

Citation:

Hanson, E. L. M., Agapitov, O. V., Mozer, F. S., Krasnoselskikh, V., Bale, S. D., Avanov, L., et al. (2020).

Terrestrial bow shock parameters from MMS measurements: Dependence on upstream and downstream time ranges. *Journal of Geophysical Research: Space Physics*, 125, e2019JA027231. <https://doi.org/10.1029/2019JA027231>

Received 30 JUL 2019

Accepted 27 NOV 2019

Accepted article online 20 DEC 2019

Terrestrial Bow Shock Parameters From MMS Measurements: Dependence on Upstream and Downstream Time Ranges

E. L. M. Hanson¹, O. V. Agapitov¹, F. S. Mozer¹, V. Krasnoselskikh^{1,2}, S. D. Bale¹, L. Avanov^{3,4}, B. L. Giles⁴, and R. B. Torbert⁵

¹Space Sciences Laboratory, University of California, Berkeley, CA, USA, ²LPC2E/CNRS-University of Orléans, Orléans, France, ³Astronomy Department, University of Maryland, College Park, MD, USA, ⁴NASA Goddard Space Flight Center, Greenbelt, MD, USA, ⁵Department of Physics, University of New Hampshire, Durham, NH, USA

Abstract We have investigated the dependence of shock parameters (speed v_{sh} , normal \hat{n} , and angle θ_{Bn}) on the choice of upstream and downstream regions for 51 bow shock crossings in Magnetospheric Multiscale (MMS) Fast Survey data. We summarize guidelines for selecting stream regions based on the magnetic field and particle moments. Preferred upstream and downstream combinations were identified by minimizing Rankine-Hugoniot conservation errors. Comparing parameters from different upstream/downstream combinations provided a measure of how stream region choices affect the parameters. Shifting from the preferred stream region combination to another would cause $<5^\circ$ change in \hat{n} for 90% of shocks, <15 km/s change in v_{sh} of 70% of shocks, and $<5^\circ$ change in θ_{Bn} for 84% of shocks. All parameters would shift by more than their standard deviations σ . The most robust is \hat{n} , which would change by $<1\sigma$ for 22% and $<3\sigma$ for 86% of shocks, while v_{sh} is the least robust, changing by $<3\sigma$ for only 12% of shocks. We provide summary plots and detailed lists of parameters in the supporting information (also available at <https://doi.org/10.5281/zenodo.3583341>).

1. Introduction

Early spacecraft observations of collisionless shocks, such as the Earth's bow shock, were limited by low data sampling rates, which made it natural to concentrate on analysis of the macroscopic features and physics (e.g., Formisano et al., 1973; Formisano et al., 1973; Formisano & Hedgecock, 1973; Kennel et al., 1985; Leroy et al., 1982). As instrument technology has advanced, providing increasingly detailed data within the shock transition, observational studies have expanded to include waves (e.g., Balikhin et al., 2005; Breneman et al., 2013; Hobara et al., 2008; Hull et al., 2006, 2012; Lobzin et al., 2005; Oka et al., 2017; Vasko et al., 2018; Walker et al., 2008; Wilson et al., 2014b; Wilson et al., 2017), electric fields (e.g., Bale et al., 2005, 2008; Bale & Mozer, 2007; Balikhin et al., 2002; Dimmock et al., 2011, 2012; Formisano, 1982; Hanson et al., 2019; Heppner et al., 1978; Hobara et al., 2010; Lefebvre et al., 2007; Scudder et al., 1986; Scudder et al., 1986; Scudder, Mangeney, Lacombe, Harvey, Wu, et al., 1986; Walker et al., 2004; Wygant et al., 1987), and nonstationarity and rippling (e.g., Burgess, 2006; Burgess & Scholer, 2007; Johlander et al., 2016; Lobzin et al., 2007; Lowe & Burgess, 2003; Ofman & Gedalin, 2013a, 2013b; Winske & Quest, 1988). Missions that have been utilized for collisionless shock studies include International Sun-Earth Explorer (e.g., Sckopke et al., 1983), INTERSHOCK (e.g., Walker et al., 1999), Active Magnetospheric Particle Tracer Explorer (e.g., Balikhin et al., 1999), Cluster (e.g., Artemyev et al., 2013; Bale et al., 2005; Kis et al., 2013; Krasnoselskikh et al., 2013; Kruparova et al., 2019), Time History of Events and Macroscale Interactions during Substorms (e.g., Hobara et al., 2010; Wilson et al., 2014a, 2014ab), Polar (e.g., Bale & Mozer, 2007; Hull et al., 2006, 2012), and Wind (e.g., Wilson et al., 2012; Wilson et al., 2017), among others. Whether a given study inclines more to the macroscopic or the microscopic view, situating a given shock within the context of previous work still involves estimation of average plasma parameters before and after the shock, in the so-called upstream and downstream regions.

Identification of the upstream and downstream regions in an idealized theoretical context, or even in a self-contained simulation environment, is a relatively straightforward matter. From an observational perspective, the low sampling rates of measurements used in early studies necessitated averaging over long periods of minutes before and after the shock (e.g., Formisano, Hedgecock, et al., 1973; Newbury et al., 1998).

Table 1*Characteristics in Summary Data That Can Guide the Selection of Appropriate Upstream and Downstream Regions for a Shock Observation*

	Upstream	Downstream
$ B $	We want to see a smooth, nearly flat approach to the ramp. Small fluctuations are unavoidable and generally innocuous, but one should avoid plateau-like formations. Subjectivity enters here in judging how high is too high for such a plateau. The gradual increase in $ B $ preceding the ramp, that is, the foot, should also be excluded when visible.	Large-amplitude fluctuations in $ B $ are normal, but if they appear periodic, they may be wave-like activity rather than random oscillations. Periodic structures indicate that the plasma has not yet reached an equilibrium downstream state. Identifying, and avoiding, any overshoot and undershoot is likewise not always simple, whence arises some of the value of comparing multiple downstream options. Any obvious, sustained rotation is to be avoided.
B	The individual components of \mathbf{B} should exhibit a smooth, flat approach to the ramp.	
Density	The ion and electron densities should be smooth and flat while nearing the ramp.	The ion and electron densities should have stabilized into a comparatively flat signal after the ramp. During the overshoot or undershoot, they may continue to rise or fall slowly; this remains a region to avoid.
Energy flux	The ion energy flux is particularly useful for refining the allowed boundaries of the upstream region. In the upstream, we want to see only the steady, comparatively narrow beam of the incoming solar wind. Features to watch out for and exclude are any significant population outside the solar wind beam energy range preceding the ramp, such as reflected ions. A similar caveat applies to the electrons, but this is rarely an issue.	The ion energy flux should settle into a broader signal, but concentrated populations of higher- or lower-energy ions may be visible near or immediately after the ramp. These will often appear correlated with irregular behavior in the temperature or density data but not necessarily with the magnetic field data, which is why it is important and useful to include the particle moments when establishing upstream and downstream boundaries.
Temperature	The ion and electron parallel and perpendicular temperatures should be flat and steady for an extended period preceding the ramp. However, irregularities rarely occur in isolation: temperature enhancements ahead of the ramp often accompany nonsolar-wind populations in the ion energy flux.	The remarks about the densities are relevant to the ion and electron temperatures, whose behavior may appear erratic for a little while after the ramp.

Advances in spacecraft measurement technology have resulted in sophisticated measurements at much higher cadences, with the curious consequence that identifying data appropriate for the upstream and downstream averages can be a dilemma. Kennel et al. remarked that analysis of jump conditions using the Rankine-Hugoniot (RH) relations required choosing two states “separated by a distance greater than the longest dissipative scale length” (1985), while Viñas and Scudder noted that no standard procedure existed for selecting data representative of the upstream and downstream states (1986).

In this paper we endeavor to collect and articulate some of the common wisdom behind such choices. We then put these guidelines into practice by selecting four possible combinations of upstream and downstream regions for each of a set of 51 shocks observed by the Magnetospheric Multiscale (MMS) mission. By comparing the shock parameters derived from different combinations of upstream and downstream regions, we seek to estimate the reliability of the parameters as well as the possible consequences of choosing different stream regions.

This report is organized as follows. In section 2, we provide a description of the MMS data used in our calculations. In section 3, we explain the RH analysis method whereby we obtained the shock geometry and parameters. In section 4, we give a general guide to selecting the boundaries of the upstream and downstream regions with respect to features seen in the summary data. In section 5, we describe the metrics we used to probe the quality of the results. In section 6, we comment on the shocks comprising the database. In section 7, we summarize the performance of our RH method on the shock database and present our conclusions. Summary plots and detailed parameter tables for each shock are provided in the supporting information (also available at <https://doi.org/10.5281/zenodo.3583341>).

2. Data

Our database consists of 51 bow shock crossings recorded by the MMS mission. MMS is made up of four spacecraft launched in March 2015 to orbit the Earth in a 3-D tetrahedral configuration, with

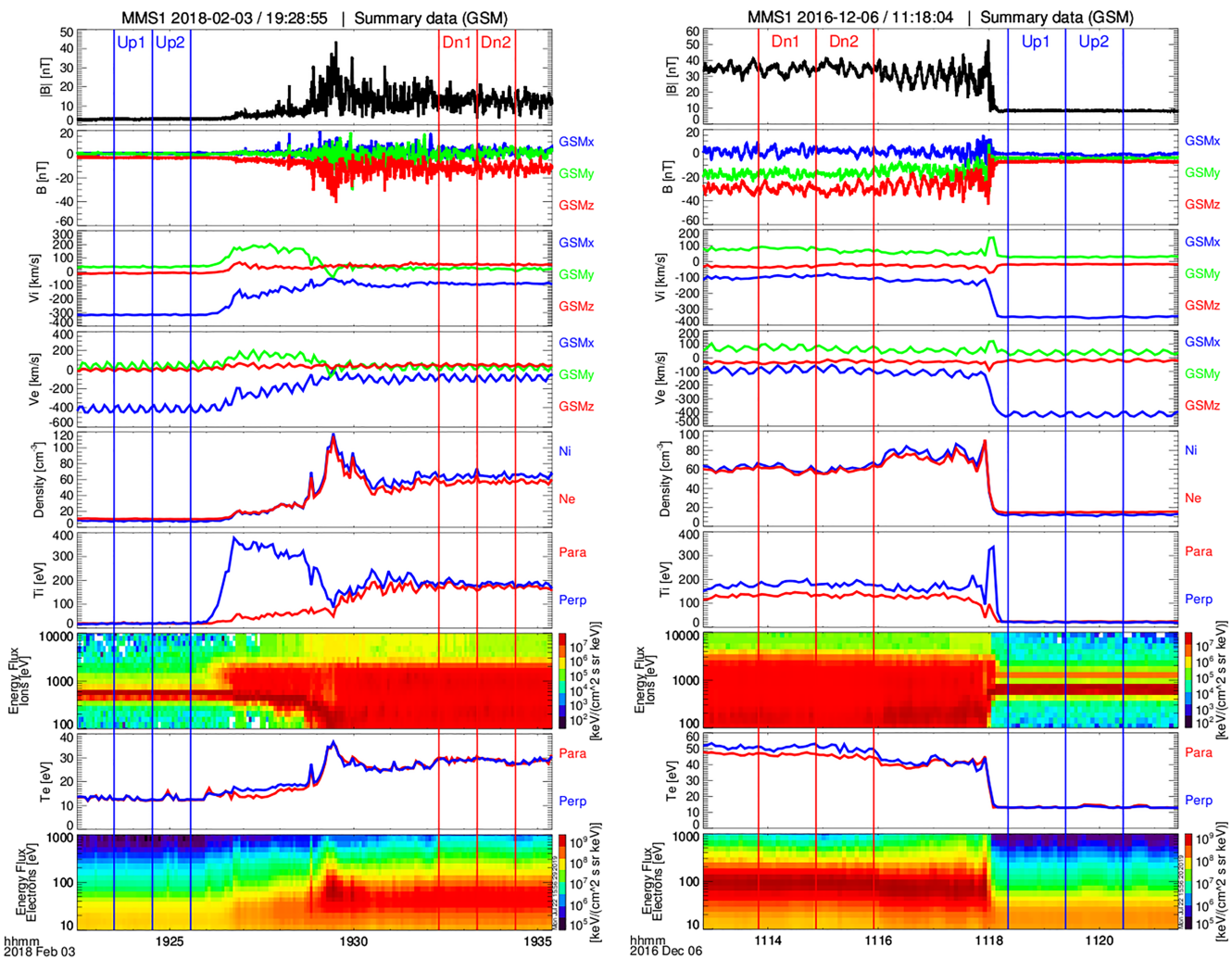


Figure 1. Summary data from MMS1 for two shocks: 3 February 2018 (left) and 06 December 2016 (right). Each shock includes the following panels from top to bottom: magnetic field magnitude, magnetic field vector, ion velocity, electron velocity, ion and electron density, ion parallel and perpendicular temperatures, ion energy flux, electron parallel and perpendicular temperatures, and electron energy flux. Vertical blue (red) lines indicate the two chosen upstream (downstream) regions, which are adjacent and nonoverlapping. The 3 February 2018 (left) shock shows a good example of a foot in the magnetic fields, accompanied by gradients in the particle moments, a strong enhancement in the ion perpendicular temperature, and the presence of an ion energy flux population distinct from and having higher energy than the incoming solar wind. The upstream regions were selected ahead of all these features. After the ramp, the magnetic fields, particle densities, and electron temperatures of the same shock show an overshoot that overlaps with an enhanced population of high-energy ions. It is less clear where the plasma has returned to its new, downstream equilibrium, but the downstream time ranges were selected to avoid the most salient features of the ramp and overshoot. In the 6 December 2016 (right) data, upstream phenomena are not so prolonged, and the upstream time regions may be situated closer to the ramp observation. However, fluctuations in the downstream magnetic field look much more likely to be oscillations in this case, so the downstream regions were chosen after these oscillations fade into a more chaotic signal.

interspacecraft separations on the order of tens of kilometers (Fuselier et al., 2016). The elliptical orbit remains within 25° of the ecliptic plane, with an early apogee of $\sim 12 R_E$ that was later increased to $25 R_E$ (Fuselier et al., 2016). Originally designed to probe reconnection physics in the vicinity of the Earth, the MMS mission has yielded a rich abundance of high-resolution data that lends itself well to probing other physics (Burch et al., 2016). We selected shock events by their magnetic field magnitude variation, and the majority of them (48 shocks or $\sim 94\%$) are reasonably robust, with a few exceptions we retained for the sake of curiosity. The particle moments were gathered by the Fast Plasma Instrument (Pollock et al., 2016), while the magnetic field measurements were taken by the Fluxgate Magnetometers (Torbert et al., 2016). In order to ensure that we had ample flexibility in our choice of upstream and downstream regions for each shock, we limited ourselves to the Fast Survey particle moments (4.5 s resolution) and magnetic

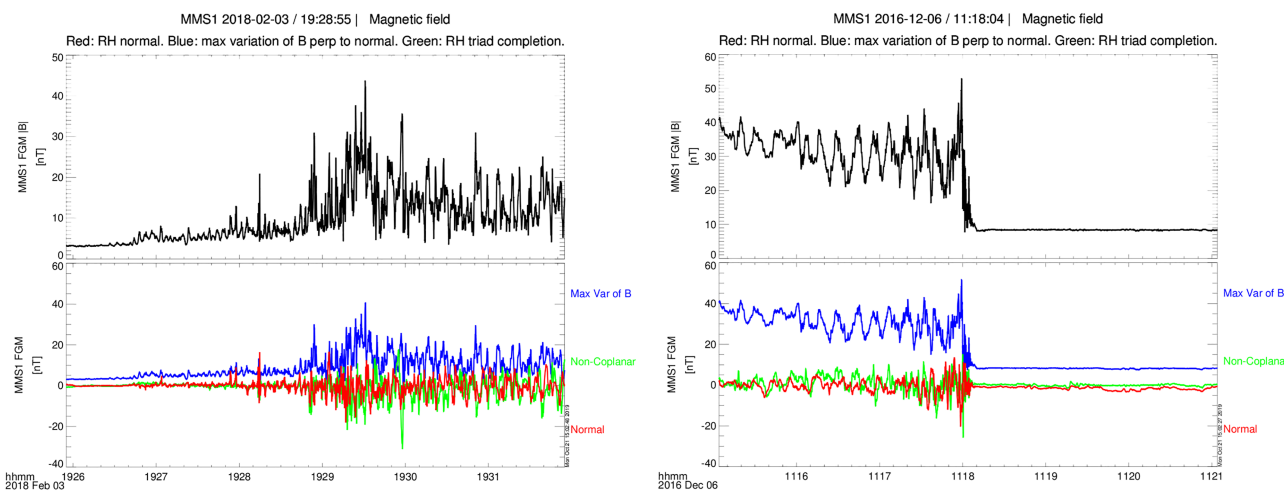


Figure 2. Magnetic field magnitude (top panels) and vector components (bottom panels) from MMS1 for the same two shocks shown in Figure 1: 3 February 2018 (left) and 6 December 2016 (right). In both plots, the bottom panel presents the magnetic field vector in a coordinate system defined by the shock normal (red) and the average upstream magnetic field component perpendicular to the shock normal (blue). The third component (green) completes the right-handed triad.

field data (62.5 ms resolution). Burst data are available for 24 of the 51 shocks, with ion moments at 150 ms, electron moments at 30 ms, and magnetic field vectors at 8 ms (Pollock et al., 2016; Torbert et al., 2016).

3. Rankine-Hugoniot Solution Method

The observations from each spacecraft, for each shock, were handled independently. Estimation of the shock parameters required the magnetic field vector dynamics, particle velocity moment vector, and particle density. We processed the electron velocity and density, because solar wind electrons form a more isotropic distribution than the beam-like solar wind ions and thus can be measured with greater reliability by electrostatic analyzers (Hanson et al., 2019).

The cadence of the electron moments (4.5 s) is longer than that of the magnetic field vectors (62.5 ms). Two adjacent groups of 1,000 time stamps (62.5 s each) were then chosen from the upstream side of the shock and also the downstream side. Thus, there were four combinations of upstream and downstream regions. For a given combination of upstream and downstream time intervals, the magnetic field minimum variance analysis normal and the Slavin and Holzer (SH) model (Slavin & Holzer, 1981) normal were computed for comparison with the RH result. All these methods of shock normal estimation are meticulously described by Schwartz in a chapter about shock geometry and parameters (Schwartz, 1998). For the cases we processed, the normals obtained from minimum variance analysis were similar to those derived from RH analysis. A limited search area, with angular resolution of 1° in azimuth and polar angles, was defined in order to lessen the risk that both orientations of the shock normal would be present within the search area, as this could introduce problematic ambiguity.

For each shock, each spacecraft, each combination of upstream and downstream intervals, and each possible pair of Geocentric Solar Magnetospheric (GSM) azimuth and polar angles in the search area, a normal vector was defined by the direction of the given azimuth and polar angle pair. The shock speed v_{sh} for each of 100 ensembles at a given azimuth and polar angle pair was computed from the continuous normal flow constraint. We checked the conservation of magnetic field and transverse momentum flux across the shock surface, but we omitted the transverse electric field (from the cross product of velocity and magnetic field) because it yielded poorly defined minima.

The errors in conservation were normalized by averages taken across both upstream and both downstream regions: Errors due to the magnetic field were normalized by the average magnetic field magnitude, while errors due to momentum flux were normalized by the sum of the average ion kinetic energy and magnetic energy. The normalized errors were rescaled to range between 0 and 1 and then added to yield a total error.

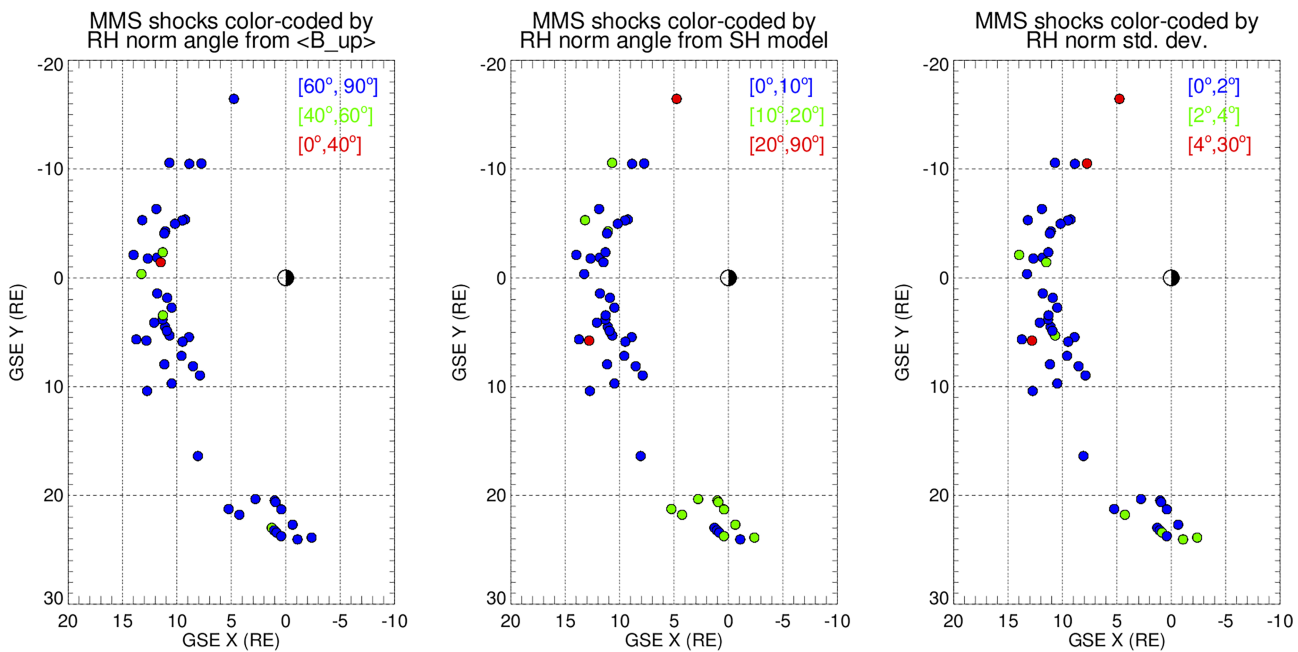


Figure 3. GSE x and y coordinates of observed bow shock crossings, in units of Earth radii. In the left panel, symbol colors indicate the angle θ_{Bn} between the shock normal and the average upstream magnetic field (dark blue: 60°–90°, green: 40°–60°, and red: 0°–40°). In the center panel, symbol colors indicate the maximum angle of deviation between the SH model normal and the preferred RH normals for each MMS probe (dark blue: 0°–10°, green: 10°–20°, and red: 20°–90°). In the right panel, symbol colors indicate the standard deviation of the preferred RH normals for the four MMS probes (dark blue: 0°–2°, green: 2°–4°, and red: 4°–30°). Larger discrepancies between the normals of each probe may indicate nonstationarity or rippling in the shock.

The average normal vector and shock speed for the ensemble was determined by identifying the minimum total error using the averages over the entire upstream and downstream ranges. With these two critical pieces of information—the shock normal and shock speed—we determined other shock and plasma parameters of interest for each pair of upstream and downstream regions, for each spacecraft, and for each shock.

4. Setting Initial Boundaries for Appropriate Stream Times

In order to choose upstream and downstream boundaries, we examined a plot of time series data with the following panels: magnetic field magnitude, magnetic field vector, ion and electron density, ion energy flux, ion parallel and perpendicular temperature, electron energy flux, and electron parallel and perpendicular temperature. For most, but not all, shocks in our database, the ramp was observed within fractions of a

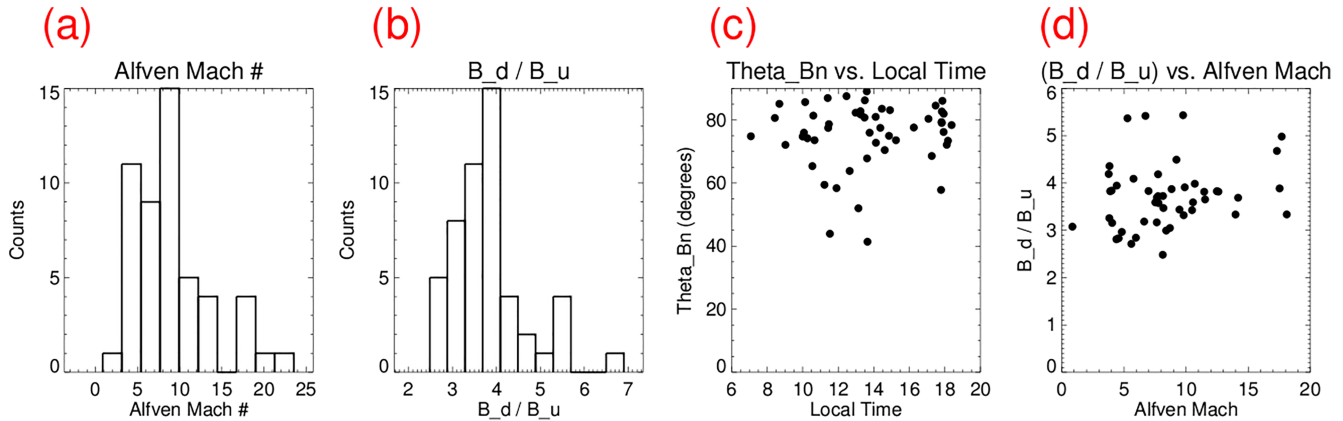


Figure 4. (a, b) Histograms showing the distribution of Alfvén Mach number (a) and downstream-to-upstream magnetic field compression ratio (b) for the full database of 51 shocks. The Alfvén Mach number is calculated in the normal incidence (NI) frame for all ions in the solar wind beam. (c, d) Scatter plots showing shock angle versus local time (c) and magnetic field compression ratio versus Alfvén Mach number (d).

Table 2
Standard Deviation of Shock Parameters for the Preferred Stream Region Combinations

Standard deviations					
Shock normal \hat{n}		Shock speed v_{sh}		Shock angle θ_{Bn}	
<3°	>3°	<10 km/s	>10 km/s	<2°	>2°
90.2%	9.8%	94.1%	5.9%	96.1%	3.9%

second by all four spacecraft. In the event that the shock ramp observations do not coincide, special care must be taken to select upstream or downstream boundaries suitable for the individual spacecraft data.

In the upstream and downstream regions alike, there are certain features that should be captured or avoided. These features are summarized in Table 1, while examples of the phenomena described are shown in Figure 1.

5. Algorithm and Metrics

In order to designate the preferred upstream and downstream combination, we judge the RH conservation error from the magnetic field and the momentum flux. For each probe, the RH conservation errors corresponding to the four upstream and downstream range combinations were compared. The minimum error and the maximum standard deviation were both identified; all errors within one standard deviation of the minimum were identified as contenders to be preferred for that probe. The number of preferred designations for each upstream/downstream combination (0 if it was not a contender for any probe, or 4 if it was a candidate for all probes) were then compared and the maximum number of preferred designations identified. Two scenarios were possible:

1. Only one upstream/downstream combination had the maximum value, which was at least 2, indicating that two or more spacecraft were in agreement as to the preferred upstream/downstream combination.
2. Two or more upstream/downstream combinations had the maximum value. Of these competing preferred combinations, the one chosen was the one that most closely sandwiched the shock ramp (near upstream and near downstream, if available). In the event that the only two viable preferred options were the near/far and far/near combinations, the preferred option was the one with the near upstream.

In this way we attempted to establish preferred upstream and downstream regions for each shock. The shock-normal magnetic field component can be seen in Figure 2, which shows the magnetic field magnitude and vector for the same shock crossings as in Figure 1. Here, the components of the magnetic field vector are defined by the shock normal direction and the average upstream magnetic field perpendicular to the shock normal, with the third component chosen to complete the right-handed triad. The normal magnetic field component stays roughly constant (on average) during the shock crossing, which indicates good estimation of the shock normal direction. Thereafter it was necessary to estimate the robustness of each shock, which we did using the shock velocity v_{sh} , θ_{Bn} , and normal deviation angle. For the shock speed v_{sh} and θ_{Bn} , we first computed the average of the absolute differences between the parameter value for the preferred stream

Table 3
The Average Change in Parameters Between the Preferred Stream Combination and the Other Combinations

Average differences				
Shock normal \hat{n}				
<2°	2–3°	3–5°	>5°	
47.1%	29.4%	13.7%	9.8%	
Shock speed v_{sh}				
<5 km/s	5–10 km/s	10–15 km/s	>15 km/s	
11.8%	35.3%	23.5%	29.4%	
Shock angle θ_{Bn}				
<2°	2–3°	3–5°	>5°	
43.1%	17.6%	23.5%	15.7%	

Table 4

The Average Change in Parameters Between the Preferred Stream Combination and the Other Combinations, Normalized by the Corresponding Standard Deviation of Each Individual Shock

Normalized average differences	<1.0	1.0–2.0	2.0–3.0	>3.0
Shock normal \hat{n}	21.6%	49.0%	15.7%	13.7%
Shock speed v_{sh}	3.9%	11.8%	5.9%	78.4%
Shock angle θ_{Bn}	7.8%	37.3%	15.7%	39.2%

combination and the parameter value for the other combinations. The average difference in the normal was estimated by averaging the deviation angle between the normal vector of the preferred upstream and downstream regions and the normal vector of the other stream region combinations. The robustness of any given parameter was taken to be the average difference normalized by the corresponding standard deviation.

6. Description of Results and Database

We selected 51 bow shock crossings observed by MMS between September 2015 and March 2018. The vast majority of shocks selected are quasi-perpendicular. All bow shock crossing locations are shown in Figure 3, where the symbols are color coded by the angle θ_{Bn} between the shock normal and the average upstream magnetic field (left panel), by the maximum angular separation between the SH normal and the preferred RH normals for the four probes (center panel), and by the standard deviation between the probes' preferred RH normals (right panel). The distribution of all shocks is illustrated in Figure 4, where the histograms on the left show the spread of Alfvén Mach number (Figure 4a) and the downstream-to-upstream ratio of the magnetic field (Figure 4b). The scatter plots on the right show shock angle plotted against local time (Figure 4c) and the magnetic field compression ratio plotted versus Alfvén Mach number (Figure 4d).

In Table A1 of the appendix, we summarize some basic parameters for each shock. More detailed parameter tables and a summary plot of each shock are given in the supporting information (also available at <https://doi.org/10.5281/zenodo.3583341>).

7. Discussion and Conclusions

The values of the parameters are of secondary interest to us in this case; we are most interested in assessing the robustness. In Tables 2–4, we have assembled a breakdown of the shock statistics by the standard deviation, average differences, and normalized differences for key parameters. The standard deviations are consistently low throughout the database; they are summarized in Table 2. The standard deviation in the normal vector is less than 3° for 90% of shocks in the database, while for over 90% of shocks, the standard deviation in the shock speed is less than 10 km/s. The standard deviation in θ_{Bn} is less than 2° for over 95% of the database. These standard deviations result solely from the analysis and do not account for experimental or instrumental sources of error.

In Table 3, the average difference thresholds are expressed in the dimensions of each parameter, representing the average shift to be expected from switching from the preferred stream region combinations to any other combination. The parameters of most shocks in the database would exhibit only modest differences if a different combination of stream regions were chosen: 90% of all shocks would experience less than 5° change in the normal vector, 71% would experience less than 15 km/s change in speed, and 85% would experience less than 5° change in shock angle.

We gain an alternative understanding by normalizing the average differences of each shock's parameters by their respective standard deviations σ , as shown in Table 4. From this perspective, it is apparent that the amount by which each shock's parameters might change are generally larger than the standard deviation, suggesting that, small absolute differences notwithstanding, a shift of the upstream and/or downstream regions produces a parameter profile that is separate and distinct. This effect is least pronounced in the case of the normal, which would remain within 1σ for 22% of shocks and within 3σ for 86%. Only 8% (60%) of shocks exhibit less than 1σ (3σ) change in θ_{Bn} . The least robust parameter is the shock speed: 78% of

shocks would change by more than 3σ if the upstream and/or downstream regions were shifted. The amount of robustness required in any given parameter depends on the intended topic of study.

Because the angular resolution of the possible normals in the RH analysis is 1° , the standard deviation in the normals must be at least 1° as well. That such a high proportion of the database has low standard deviations (less than 3° for the normal, less than 10 km/s for the speed, and less than 2° for the shock angle) provides a reassuring testimonial to the utility of RH analysis for our purposes. Of greater interest in the context of this paper are the consistently low average differences in all parameters across the database, which indicate that little change is to be expected from selecting different preferred stream regions for the majority of shocks in the database. While this is reassuring, some visual attention is still required when designating boundaries for upstream and downstream regions, and the strategy outlined in Table 1 may be helpful. Having chosen a shock for further study, performing RH analysis on an ensemble of randomly chosen points will typically yield parameters that are self-consistent within reasonably small errors. Instrumental and systematic effects must be taken into account separately, while comparison of a few stream region combinations helps not only to identify optimal upstream/downstream combinations but also to confirm the robustness of the parameters. Given that our database is strongly skewed toward quasi-perpendicular shocks, it could be interesting to repeat a similar investigation on a set of quasi-parallel shocks.

Appendix A

Table A1 presents a summary of basic parameters obtained by performing RH analysis on the preferred upstream and downstream regions for each shock in our database.

Table A1
Summary of Parameters for the Preferred Upstream and Downstream Combination for Each of the 51 Shocks

Shock time	\hat{n} GSM RH	$\alpha_{RH,SH}$	$\langle v_{sh} \rangle$	$\langle \theta_{Bn} \rangle$	Normalized differences		
	N/A	(deg)	(km/s)	(deg)	\hat{n}	v_{sh}	θ_{Bn}
2015-10-07/12:07:12	(0.888, 0.328, -0.321)	5.0	12.7 ± 1.7	73.6 ± 1.0	1.347	3.364	1.347
2015-10-21/10:52:50	(0.951, 0.189, -0.246)	4.8	11.6 ± 1.9	83.5 ± 1.0	1.360	15.752	2.751
2015-11-03/09:19:58	(0.998, -0.009, 0.070)	8.4	140.4 ± 3.9	38.8 ± 1.0	2.090	3.427	1.244
2015-11-13/13:58:25	(0.977, 0.116, -0.178)	8.8	4.5 ± 1.7	80.8 ± 1.0	1.523	11.078	2.724
2015-11-29/11:31:48	(0.990, 0.087, -0.109)	1.8	9.5 ± 1.7	82.6 ± 1.0	1.684	2.465	1.470
2015-12-10/05:25:39	(0.994, -0.091, -0.052)	1.3	8.9 ± 1.3	87.0 ± 1.0	0.881	15.856	1.221
2015-12-20/00:04:56	(0.966, -0.214, -0.143)	6.2	142.2 ± 2.1	74.7 ± 1.0	1.020	12.164	1.206
2015-12-20/00:24:57	(0.969, -0.197, -0.148)	6.8	20.1 ± 1.6	76.0 ± 1.0	0.958	5.038	5.390
2015-12-20/01:24:53	(0.988, -0.152, -0.031)	6.5	32.5 ± 1.6	74.2 ± 1.0	1.276	3.484	1.813
2015-12-22/07:14:44	(0.989, -0.130, -0.065)	3.3	74.5 ± 1.3	59.4 ± 1.0	1.701	16.016	3.403
2015-12-28/05:07:17	(0.995, 0.022, -0.096)	14.3	-24.0 ± 1.1	81.4 ± 1.0	5.153	10.166	3.247
2016-11-09/12:58:05	(0.971, 0.193, -0.139)	9.6	-20.5 ± 1.2	84.1 ± 1.0	6.763	13.566	5.101
2016-12-05/12:46:10	(0.969, 0.228, -0.096)	4.8	4.4 ± 1.5	75.9 ± 1.0	0.736	3.597	1.356
2016-12-06/11:18:04	(0.996, 0.091, 0.017)	5.7	30.2 ± 1.6	80.7 ± 1.0	2.535	7.338	5.055
2016-12-06/12:04:27	(0.993, 0.100, 0.061)	6.3	256.5 ± 3.8	89.4 ± 1.0	1.338	12.246	2.112
2016-12-07/15:16:26	(0.941, 0.338, -0.031)	2.2	-2.4 ± 1.4	72.7 ± 1.0	2.207	4.730	1.652
2016-12-09/10:43:20	(0.992, 0.117, 0.035)	2.4	-10.7 ± 1.9	82.6 ± 1.0	1.609	13.887	3.691
2016-12-17/12:06:48	(0.980, 0.199, -0.009)	1.5	0.7 ± 1.0	52.0 ± 1.0	2.561	4.333	2.038
2016-12-31/06:08:33	(0.998, -0.057, 0.004)	1.3	34.5 ± 6.0	37.9 ± 1.0	1.826	11.725	9.643
2016-12-31/12:39:33	(1.000, 0.004, 0.031)	4.9	38.9 ± 1.1	63.8 ± 1.0	3.128	17.829	1.565
2017-01-18/05:38:50	(0.990, -0.117, 0.074)	7.2	25.0 ± 1.4	73.6 ± 1.0	3.345	14.581	11.030
2017-10-03/20:34:57 ^a	(0.923, 0.382, -0.052)	16.9	-110.5 ± 2.7	79.3 ± 1.0	2.268	3.803	2.566
2017-10-03/20:52:30 ^a	(0.876, 0.481, -0.044)	11.4	-83.6 ± 2.9	82.6 ± 1.0	1.508	3.619	1.011
2017-10-09/18:13:51 ^a	(0.811, 0.584, 0.035)	7.2	-59.6 ± 4.2	57.4 ± 1.0	1.661	1.772	4.043
2017-10-09/19:04:23	(0.805, 0.590, -0.052)	6.0	-48.1 ± 2.9	79.0 ± 1.0	1.405	2.516	3.168
2017-10-09/19:54:30 ^a	(0.824, 0.566, 0.009)	8.5	-75.1 ± 3.5	86.1 ± 1.0	0.824	2.036	1.334
2017-10-09/21:32:54 ^a	(0.827, 0.563, 0.004)	9.4	-45.7 ± 3.1	81.9 ± 1.0	1.033	3.207	4.543
2017-10-10/08:11:53 ^a	(0.860, 0.486, -0.156)	13.9	-87.1 ± 3.5	78.3 ± 1.0	1.020	4.303	7.964
2017-10-13/03:08:10 ^a	(0.789, 0.611, -0.065)	6.7	-81.2 ± 4.5	73.4 ± 1.0	0.922	1.991	2.696
2017-10-18/01:39:37 ^a	(0.893, 0.441, -0.087)	10.0	-59.8 ± 2.6	82.2 ± 1.0	1.705	4.124	4.769

Table A1
(continued)

Shock time	\hat{n} GSM RH	$\alpha_{RH,SH}$	$\langle v_{sh} \rangle$	$\langle \theta_{Bn} \rangle$	Normalized differences		
	N/A	(deg)	(km/s)	(deg)	\hat{n}	v_{sh}	θ_{Bn}
2017-10-19/00:56:54	(0.880, 0.473, 0.044)	15.8	-87.6 ± 2.6	72.1 ± 1.0	0.874	1.319	2.982
2017-10-24/20:03:13	(0.761, 0.558, 0.330)	15.7	279.1 ± 3.8	76.3 ± 1.0	3.288	10.062	3.090
2017-11-02/04:26:45	(0.903, 0.430, -0.009)	11.3	-49.3 ± 3.1	68.6 ± 1.0	0.650	1.871	1.193
2017-11-02/08:29:22	(0.899, 0.400, -0.178)	13.7	-5.1 ± 2.8	84.8 ± 1.0	1.965	5.020	4.271
2017-11-14/19:57:09	(0.958, 0.279, -0.070)	8.9	36.9 ± 2.3	70.4 ± 1.0	3.382	5.465	1.972
2017-11-25/01:26:12	(0.945, 0.321, 0.061)	9.0	-23.4 ± 1.9	77.6 ± 1.0	2.033	7.391	4.653
2017-11-25/23:40:01	(0.900, 0.183, -0.395)	28.9	5.6 ± 6.8	67.9 ± 2.4	0.116	0.353	0.783
2017-11-28/18:00:56	(0.988, 0.156, 0.013)	4.2	-18.1 ± 1.2	81.7 ± 1.0	0.583	6.254	0.248
2017-12-23/10:44:52	(0.963, 0.267, 0.035)	8.4	-4.8 ± 1.3	75.0 ± 1.0	2.226	4.046	1.678
2017-12-26/22:09:12	(0.986, -0.161, 0.035)	2.4	-7.7 ± 1.1	78.6 ± 1.0	1.614	8.871	3.992
2017-12-31/22:09:33	(0.910, 0.331, 0.250)	3.7	19.2 ± 1.7	77.7 ± 1.0	1.269	3.967	1.924
2018-01-12/03:22:34	(0.986, 0.052, 0.156)	5.4	-23.7 ± 1.7	86.2 ± 1.0	1.976	4.370	1.414
2018-01-18/11:50:38	(0.964, -0.254, 0.074)	3.4	-7.8 ± 1.3	88.5 ± 1.0	1.416	10.142	5.046
2018-02-03/19:28:55	(0.987, -0.052, 0.152)	1.5	-8.7 ± 1.4	89.4 ± 1.0	1.121	4.154	0.599
2018-02-07/06:50:30	(0.945, -0.325, -0.022)	10.1	-41.9 ± 1.8	72.1 ± 1.0	1.256	4.782	1.905
2018-02-09/09:18:58	(0.969, 0.042, 0.242)	7.5	-11.2 ± 1.4	58.0 ± 1.0	4.665	4.615	2.598
2018-02-10/01:00:58	(0.887, -0.452, -0.092)	1.9	-13.8 ± 2.0	85.2 ± 1.0	1.720	1.581	1.744
2018-02-12/20:02:14	(0.899, -0.419, -0.131)	7.9	-42.6 ± 18.6	80.6 ± 13.5	0.362	0.622	0.161
2018-02-14/23:48:09	(0.978, -0.094, 0.187)	7.6	-14.8 ± 1.4	77.5 ± 1.0	0.886	3.292	1.849
2018-03-01/01:43:11	(0.977, -0.163, -0.139)	12.6	-8.5 ± 1.3	65.4 ± 1.0	2.139	9.417	3.767
2018-03-13/04:52:28	(0.536, 0.773, 0.338)	82.1	-188.6 ± 2.1	74.8 ± 1.4	1.456	1.764	6.277

Note. Columns from left to right hold the shock time; the GSM components of the RH normal, averaged over the four spacecraft; angle between the RH and SH normals; shock speed; shock angle θ_{Bn} ; and normalized differences of the normal, shock speed, and shock angle expressed in units of the standard deviations of each parameter. Dates in the first column are formatted as YYYY-MM-DD.

^aThe ramp observation time for the four spacecraft differs by more than a few seconds.

Acknowledgments

The authors thank the entire MMS team for providing such excellent data, which is publicly available online (at <https://lasp.colorado.edu/mms/sdc/public/about/how-to/>). The authors thank I.Y. Vasko, K. A. Goodrich, and S. J. Schwartz for fruitful discussion. Work at UC Berkeley benefited from the support of NASA Contract NNN06AA01C. The supporting information for this paper is also available in a public repository (at <https://doi.org/10.5281/zenodo.3583341>).

References

- Artyeyev, A. V., Agapitov, O. V., & Krasnoselskikh, V. V. (2013). Cyclotron resonance in plasma flow. *Physics of Plasmas*, 20(12), 124502. <https://doi.org/10.1063/1.4853615>
- Bale, S. D., Balikhin, M. A., Horbury, T. S., Krasnoselskikh, V. V., Kucharek, H., Möbius, E., et al. (2005). Quasi-perpendicular shock structure and processes. *Space Science Reviews*, 118(1–4), 161–203. <https://doi.org/10.1007/s11214-005-3827-0>
- Bale, S. D., & Mozer, F. S. (2007). Measurement of large parallel and perpendicular electric fields on electron spatial scales in the terrestrial bow shock. *Physical Review Letters*, 98(20). <https://doi.org/10.1103/PhysRevLett.98.205001>
- Bale, S. D., Mozer, F. S., & Krasnoselskikh, V. V. (2008). Direct measurement of the cross-shock electric potential at low plasma beta, quasi-perpendicular bow shocks. *ArXiv:0809.2435 [Astro-Ph, Physics: Physics]*. Retrieved from <http://arxiv.org/abs/0809.2435>
- Balikhin, M., Walker, S., Treumann, R., Alleyne, H., Krasnoselskikh, V., Gedalin, M., et al. (2005). Ion sound wave packets at the quasi-perpendicular shock front. *Geophysical Research Letters*, 32, L24106. <https://doi.org/10.1029/2005GL024660>
- Balikhin, M. A., Alleyne, H. S.-C. K., Treumann, R. A., Nozdrachev, M. N., Walker, S. N., & Baumjohann, W. (1999). The role of nonlinear interaction in the formation of LF whistler turbulence upstream of a quasi-perpendicular shock. *Journal of Geophysical Research*, 104(A6), 12525–12535. <https://doi.org/10.1029/1998JA900102>
- Balikhin, M. A., Nozdrachev, M., Dunlop, M., Krasnoselskikh, V., Walker, S. N., Alleyne, H. S. C. K., et al. (2002). Observation of the terrestrial bow shock in quasi-electrostatic subshock regime: Quasi-electrostatic subshock. *Journal of Geophysical Research*, 107(A8), 1155. <https://doi.org/10.1029/2001JA000327>
- Breneman, A. W., Cattell, C. A., Kersten, K., Paradise, A., Schreiner, S., Kellogg, P. J., et al. (2013). STEREO and Wind observations of intense cyclotron harmonic waves at the Earth's bow shock and inside the magnetosheath: Bow shock cyclotron harmonic waves. *Journal of Geophysical Research: Space Physics*, 118, 7654–7664. <https://doi.org/10.1002/2013JA019372>
- Burch, J. L., Moore, T. E., Torbert, R. B., & Giles, B. L. (2016). Magnetospheric Multiscale overview and science objectives. *Space Science Reviews*, 199(1–4), 5–21. <https://doi.org/10.1007/s11214-015-0164-9>
- Burgess, D. (2006). Simulations of electron acceleration at collisionless shocks: The effects of surface fluctuations. *The Astrophysical Journal*, 653(1), 316–324. <https://doi.org/10.1086/508805>
- Burgess, D., & Scholer, M. (2007). Shock front instability associated with reflected ions at the perpendicular shock. *Physics of Plasmas*, 14(1), 012108. <https://doi.org/10.1063/1.2435317>
- Dimmock, A. P., Balikhin, M. A., & Hobara, Y. (2011). Comparison of three methods for the estimation of cross-shock electric potential using Cluster data. *Annales Geophysicae*, 29(5), 815–822. <https://doi.org/10.5194/angeo-29-815-2011>
- Dimmock, A. P., Balikhin, M. A., Krasnoselskikh, V. V., Walker, S. N., Bale, S. D., & Hobara, Y. (2012). A statistical study of the cross-shock electric potential at low Mach number, quasi-perpendicular bow shock crossings using Cluster data: Cross-shock potential at the terrestrial bow shock. *Journal of Geophysical Research*, 117, A02210. <https://doi.org/10.1029/2011JA017089>

- Formisano, V. (1982). Measurement of the potential drop across the Earth's collisionless bow shock. *Geophysical Research Letters*, 9(9), 1033–1036. <https://doi.org/10.1029/GL009i009p01033>
- Formisano, V., & Hedgecock, P. C. (1973). Solar wind interaction with the Earth's magnetic field: 3. On the Earth's bow shock structure. *Journal of Geophysical Research*, 78(19), 3745–3760. <https://doi.org/10.1029/JA078i019p03745>
- Formisano, V., Hedgecock, P. C., Moreno, G., Palmiotto, F., & Chao, J. K. (1973). Solar wind interaction with the Earth's magnetic field: 2. Magnetohydrodynamic bow shock. *Journal of Geophysical Research*, 78(19), 3731–3744. <https://doi.org/10.1029/JA078i019p03731>
- Formisano, V., Moreno, G., Palmiotto, F., & Hedgecock, P. C. (1973). Solar wind interaction with the Earth's magnetic field: 1. Magnetosheath. *Journal of Geophysical Research*, 78(19), 3714–3730. <https://doi.org/10.1029/JA078i019p03714>
- Fuselier, S. A., Lewis, W. S., Schiff, C., Ergun, R., Burch, J. L., Petrinec, S. M., & Trattner, K. J. (2016). Magnetospheric Multiscale science mission profile and operations. *Space Science Reviews*, 199(1–4), 77–103. <https://doi.org/10.1007/s11214-014-0087-x>
- Hanson, E. L. M., Agapitov, O. V., Mozer, F. S., Krasnoselskikh, V., Bale, S. D., Avanov, L., et al. (2019). Cross-shock potential in rippled versus planar quasi-perpendicular shocks observed by MMS. *Geophysical Research Letters*, 46, 2381–2389. <https://doi.org/10.1029/2018GL080240>
- Heppner, J. P., Maynard, N. C., & Aggson, T. L. (1978). Early results from ISEE-1 electric field measurements. *Space Science Reviews*, 22(6), 777–789. <https://doi.org/10.1007/BF00212623>
- Hobara, Y., Balikhin, M., Krasnoselskikh, V., Gedalin, M., & Yamagishi, H. (2010). Statistical study of the quasi-perpendicular shock ramp widths: Shock ramp width. *Journal of Geophysical Research*, 115, A11106. <https://doi.org/10.1029/2010JA015659>
- Hobara, Y., Walker, S. N., Balikhin, M., Pokhotelov, O. A., Gedalin, M., Krasnoselskikh, V., et al. (2008). Cluster observations of electrostatic solitary waves near the Earth's bow shock: Electrostatic solitary waves. *Journal of Geophysical Research*, 113, A05211. <https://doi.org/10.1029/2007JA012789>
- Hull, A. J., Larson, D. E., Wilber, M., Scudder, J. D., Mozer, F. S., Russell, C. T., & Bale, S. D. (2006). Large-amplitude electrostatic waves associated with magnetic ramp substructure at Earth's bow shock. *Geophysical Research Letters*, 33, L15104. <https://doi.org/10.1029/2005GL025564>
- Hull, A. J., Muschietti, L., Oka, M., Larson, D. E., Mozer, F. S., Chaston, C. C., et al. (2012). Multiscale whistler waves within Earth's perpendicularly bow shock: Whistler waves at Earth's bow shock. *Journal of Geophysical Research*, 117, A12104. <https://doi.org/10.1029/2012JA017870>
- Johlander, A., Schwartz, S. J., Vaivads, A., Khotyaintsev, Y. V., Gingell, I., Peng, I. B., et al. (2016). Rippled quasiperpendicular shock observed by the Magnetospheric Multiscale spacecraft. *Physical Review Letters*, 117(16), 165101. <https://doi.org/10.1103/PhysRevLett.117.165101>
- Kennel, C. F., Edmiston, J. P., & Hada, T. (1985). In R. G. Stone & B. T. Tsurutani (Eds.), *A quarter century of collisionless shock research, Geophysical Monograph Series* (pp. 1–36). Washington, D. C.: American Geophysical Union. <https://doi.org/10.1029/GM034p0001>
- Kis, A., Agapitov, O., Krasnoselskikh, V., Khotyaintsev, Y. V., Dandouras, I., Lemperger, I., & Wesztergom, V. (2013). Gyrosurfing acceleration of ions in front of Earth's quasi-parallel bow shock. *The Astrophysical Journal*, 771(1), 4. <https://doi.org/10.1088/0004-637X/771/1/4>
- Krasnoselskikh, V., Balikhin, M., Walker, S. N., Schwartz, S., Sundkvist, D., Lobzin, V., et al. (2013). The dynamic quasiperpendicular shock: Cluster discoveries. *Space Science Reviews*, 178(2–4), 535–598. <https://doi.org/10.1007/s11214-013-9972-y>
- Kruparova, O., Krupar, V., Safránková, J., Němcéek, Z., Maksimovic, M., Santolík, O., et al. (2019). Statistical survey of the terrestrial bow shock observed by the Cluster spacecraft. *Journal of Geophysical Research: Space Physics*, 124, 1539–1547. <https://doi.org/10.1029/2018JA026272>
- Lefebvre, B., Schwartz, S. J., Fazakerley, A. F., & Décréau, P. (2007). Electron dynamics and cross-shock potential at the quasi-perpendicular Earth's bow shock: Electron dynamics and shock potential. *Journal of Geophysical Research*, 112, A09212. <https://doi.org/10.1029/2007JA012277>
- Leroy, M. M., Winske, D., Goodrich, C. C., Wu, C. S., & Papadopoulos, K. (1982). The structure of perpendicular bow shocks. *Journal of Geophysical Research*, 87(A7), 5081–5094. <https://doi.org/10.1029/JA087iA07p05081>
- Lobzin, V. V., Krasnoselskikh, V. V., Bosqued, J.-M., Pinçon, J.-L., Schwartz, S. J., & Dunlop, M. (2007). Nonstationarity and reformation of high-Mach-number quasiperpendicular shocks: Cluster observations: Shock front reformation. *Geophysical Research Letters*, 34, L05107. <https://doi.org/10.1029/2006GL029095>
- Lobzin, V. V., Krasnoselskikh, V. V., Schwartz, S. J., Cairns, I., Lefebvre, B., Décréau, P., & Fazakerley, A. (2005). Generation of downshifted oscillations in the electron foreshock: A loss-cone instability: Generation of downshifted oscillations. *Geophysical Research Letters*, 32, L18101. <https://doi.org/10.1029/2005GL023563>
- Lowe, R. E., & Burgess, D. (2003). The properties and causes of rippling in quasi-perpendicular collisionless shock fronts. *Annales Geophysicae*, 21(3), 671–679. <https://doi.org/10.5194/angeo-21-671-2003>
- Newbury, J. A., Russell, C. T., & Gedalin, M. (1998). The ramp widths of high-Mach-number, quasi-perpendicular collisionless shocks. *Journal of Geophysical Research*, 103(A12), 29581–29593. <https://doi.org/10.1029/1998JA000024>
- Ofman, L., & Gedalin, M. (2013a). Rippled quasi-perpendicular collisionless shocks: Local and global normals: Rippled shocks: Local and global normals. *Journal of Geophysical Research: Space Physics*, 118, 5999–6006. <https://doi.org/10.1029/2013JA018780>
- Ofman, L., & Gedalin, M. (2013b). Two-dimensional hybrid simulations of quasi-perpendicular collisionless shock dynamics: Gyrating downstream ion distributions: 2D hybrid models of collisionless shocks. *Journal of Geophysical Research: Space Physics*, 118, 1828–1836. <https://doi.org/10.1029/2012JA018188>
- Oka, M., Wilson, L. B. III, Phan, T. D., Hull, A. J., Amano, T., Hoshino, M., et al. (2017). Electron scattering by high-frequency whistler waves at Earth's bow shock. *The Astrophysical Journal*, 842(2), L11. <https://doi.org/10.3847/2041-8213/aa7759>
- Pollock, C., Moore, T., Jacques, A., Burch, J., Gliese, U., Saito, Y., et al. (2016). Fast plasma investigation for Magnetospheric Multiscale. *Space Science Reviews*, 199(1–4), 331–406. <https://doi.org/10.1007/s11214-016-0245-4>
- Schwartz, S. J. (1998). Shock and discontinuity normals, Mach numbers, and related parameters. In G. Paschmann & P. W. Daly (Eds.), *Analysis methods for multi-spacecraft data* (pp. 249–270). Noordwijk, The Netherlands: The International Space Science Institute.
- Sckopke, N., Paschmann, G., Bame, S. J., Gosling, J. T., & Russell, C. T. (1983). Evolution of ion distributions across the nearly perpendicular bow shock: Specularly and non-specularly reflected-gyrating ions. *Journal of Geophysical Research*, 88(A8), 6121. <https://doi.org/10.1029/JA088iA08p06121>
- Scudder, J. D., Mangeney, A., Lacombe, C., Harvey, C. C., & Aggson, T. L. (1986). The resolved layer of a collisionless, high β , supercritical, quasi-perpendicular shock wave, 2. Dissipative fluid electrodynamics. *Journal of Geophysical Research*, 91(A10), 11053. <https://doi.org/10.1029/JA091iA10p11053>

- Scudder, J. D., Mangeney, A., Lacombe, C., Harvey, C. C., Aggson, T. L., Anderson, R. R., et al. (1986). The resolved layer of a collisionless, high β , supercritical, quasi-perpendicular shock wave: 1. Rankine-Hugoniot geometry, currents, and stationarity. *Journal of Geophysical Research*, 91(A10), 11019. <https://doi.org/10.1029/JA091iA10p11019>
- Scudder, J. D., Mangeney, A., Lacombe, C., Harvey, C. C., Wu, C. S., & Anderson, R. R. (1986). The resolved layer of a collisionless, high β , supercritical, quasi-perpendicular shock wave: 3. Vlasov electrodynamics. *Journal of Geophysical Research*, 91(A10), 11075. <https://doi.org/10.1029/JA091iA10p11075>
- Slavin, J. A., & Holzer, R. E. (1981). Solar wind flow about the terrestrial planets 1. Modeling bow shock position and shape. *Journal of Geophysical Research*, 86(A13), 11401. <https://doi.org/10.1029/JA086iA13p11401>
- Torbert, R. B., Russell, C. T., Magnes, W., Ergun, R. E., Lindqvist, P.-A., LeContel, O., et al. (2016). The FIELDS instrument suite on MMS: Scientific objectives, measurements, and data products. *Space Science Reviews*, 199(1–4), 105–135. <https://doi.org/10.1007/s11214-014-0109-8>
- Vasko, I. Y., Mozer, F. S., Krasnoselskikh, V. V., Artemyev, A. V., Agapitov, O. V., Bale, S. D., et al. (2018). Solitary waves across supercritical quasi-perpendicular shocks: Solitary waves and electron isotropization. *Geophysical Research Letters*, 45, 5809–5817. <https://doi.org/10.1029/2018GL077835>
- Viñas, A. F., & Scudder, J. D. (1986). Fast and optimal solution to the “Rankine-Hugoniot problem”. *Journal of Geophysical Research*, 91(A1), 39. <https://doi.org/10.1029/JA091iA01p00039>
- Walker, S. N., Alleyne, H. S. C. K., Balikhin, M. A., André, M., & Horbury, T. S. (2004). Electric field scales at quasi-perpendicular shocks. *Annales Geophysicae*, 22(7), 2291–2300. <https://doi.org/10.5194/angeo-22-2291-2004>
- Walker, S. N., Balikhin, M. A., Alleyne, H. S. C. K., Hobara, Y., André, M., & Dunlop, M. W. (2008). Lower hybrid waves at the shock front: A reassessment. *Annales Geophysicae*, 26(3), 699–707. <https://doi.org/10.5194/angeo-26-699-2008>
- Walker, S. N., Balikhin, M. A., & Nozdrachev, M. N. (1999). Ramp nonstationarity and the generation of whistler waves upstream of a strong quasiperpendicular shock. *Geophysical Research Letters*, 26(10), 1357–1360. <https://doi.org/10.1029/1999GL900210>
- Wilson, L. B. III, Koval, A., Szabo, A., Breneman, A., Cattell, C. A., Goetz, K., et al. (2012). Observations of electromagnetic whistler precursors at supercritical interplanetary shocks: Whistler precursors-particles. *Geophysical Research Letters*, 39, L08109. <https://doi.org/10.1029/2012GL051581>
- Wilson, L. B. III, Koval, A., Szabo, A., Stevens, M. L., Kasper, J. C., Cattell, C. A., & Krasnoselskikh, V. V. (2017). Revisiting the structure of low-Mach number, low-beta, quasi-perpendicular shocks: Shock structure. *Journal of Geophysical Research: Space Physics*, 122, 9115–9133. <https://doi.org/10.1002/2017JA024352>
- Wilson, L. B. III, Sibeck, D. G., Breneman, A. W., Contel, O. L., Cully, C., Turner, D. L., et al. (2014a). Quantified energy dissipation rates in the terrestrial bow shock: 1. Analysis techniques and methodology. *Journal of Geophysical Research: Space Physics*, 119, 6455–6474. <https://doi.org/10.1002/2014JA019929>
- Wilson, L. B. III, Sibeck, D. G., Breneman, A. W., Contel, O. L., Cully, C., Turner, D. L., et al. (2014b). Quantified energy dissipation rates in the terrestrial bow shock: 2. Waves and dissipation: WILSON ET AL. *Journal of Geophysical Research: Space Physics*, 119, 6475–6495. <https://doi.org/10.1002/2014JA019930>
- Winske, D., & Quest, K. B. (1988). Magnetic field and density fluctuations at perpendicular supercritical collisionless shocks. *Journal of Geophysical Research*, 93(A9), 9681. <https://doi.org/10.1029/JA093iA09p09681>
- Wygant, J. R., Bensadoun, M., & Mozer, F. S. (1987). Electric field measurements at subcritical, oblique bow shock crossings. *Journal of Geophysical Research*, 92(A10), 11109. <https://doi.org/10.1029/JA092iA10p11109>